scientific reports

Check for updates

OPEN

Therapeutic effect of pH responsive Magainin II modified azithromycin plus curcumin micelles in different depth models of MRSA infection

Lu Zhang[1,2], Rui-bo Guo[1,2], Yang Liu[1,2], Liang Kong[1,2], Juan Zang[1,2], Zi-xu Zhang[1,2], Jia-hua Wang[1,2], Mu-han Chen[1,2], Mo Liu[1,2], Yang Yu[1,2,3]✉ & Xue-tao Li[1,2]✉

Methicillin-resistant Staphylococcus aureus **(MRSA) is a major pathogen responsible for serious infections in humans. The overuse of antibiotics has led to the evolution of resistance genes in bacteria. This study aimed to develop a pH-responsive micelle, loaded with therapy drugs and modified with antimicrobial peptides, to treat drug-resistant bacterial infections at varying depths. pH-responsive micelles containing azithromycin and curcumin, modified with Magainin II, were prepared using the thin-film dispersion method. The physicochemical properties of the micelles were characterized, and their targeting properties and therapeutic effects on bacterial infections were investigated both in vivo and in vitro across various depths. The micelles demonstrated excellent targeting of bacterial infection sites and released drugs in response to degradation at the disease site. The combination of curcumin and azithromycin effectively mitigated bacterial resistance through multiple mechanisms, enhancing the antibacterial effect while reducing the required azithromycin dosage and associated toxicity. In infection models of varying depths—skin, muscle, and lungs—the micelles exhibited strong antibacterial, anti-biofilm, and anti-inflammatory effects with low toxicity. These findings provide a promising strategy for addressing drug-resistant bacterial infections.**

Keywords MRSA, Curcumin, Active targeting, Polymer micelle, Environmental response

Bacterial infections occur when pathogenic or opportunistic bacteria invade the blood circulation, producing toxins and other metabolites. They are the second leading cause of death globally, following heart disease, with *Staphylococcus aureus* being a particularly deadly pathogen[1–3]. Since their discovery in the last century, antibiotics have been crucial in preventing and treating bacterial infections[4]. However, the widespread antibiotic use has led to the evolution of bacterial resistance genes. Bacteria accumulate in the slightly acidic microenvironment to form biofilms, which play a key role in many persistent and chronic bacterial infections[5–7]. Drug-resistant bacterial infections can occur at different depths in the body[8–10], posing a global public health challenge that necessitates the urgent development of new antimicrobial agents or effective drug delivery systems.

Antibiotic therapy remains a common approach in the clinical treatment of drug-resistant bacteria[11]. Azithromycin (AZI) is a semi-synthetic macrolide antibiotic with a 15-membered ring structure; this is widely used in clinical practice due to its broad-spectrum antibacterial activity[12,13]. However, treating resistant bacterial infections often requires higher doses of AZI, resulting in reduced bioavailability and increased toxicity. To address these issues and enhance therapeutic effects while minimizing side effects, we selected another drug to use in combination with AZI. Curcumin (Cur), derived from the rhizome of *Curcuma longa* L., exhibits a wide range of pharmacological activities, including anti-inflammatory, anti-infective, and antiviral properties. Its low toxicity and minimal side effects[14–17] make it an ideal candidate for combination therapy with antibiotics.

However, both AZI and Cur face challenges such as poor water solubility, low bioavailability, and limited stability. Among the various emerging drug delivery systems, polymer micelles (Ms) have garnered increasing attention for their ability to significantly enhance the solubility of hydrophobic drugs[18,19]. Poly(2-(diisopropyl amino)ethyl methacrylate) (PDPA) is a pH-responsive polymer[20,21]. When the pH drops below its pK_a, PDPA

[1]School of Pharmacy, Liaoning University of Traditional Chinese Medicine, Shengming 1 Road 77, Double D Port, Dalian 116600, China. [2]Shenyang Key Laboratory of Targeted Delivery of Chinese Medicine, Shenyang 110000, China. [3]Key Laboratory of Ministry of Education for TCM Viscera-State Theory and Applications, Shenyang 110000, China. ✉email: yuqn0702@163.com; lixuetao1979@163.com

becomes hydrophilic due to the protonation of diisopropyl tertiary amines[22,23]. This property makes PDPA an excellent carrier for locally delivering drugs specifically to the acidic microenvironment of bacterial infections.

In clinical settings, bacterial infections often occur at sites such as the skin, mucous membranes, muscles, tissues, and organs[8–10]. However, the variations in depth, blood vessel density, and blood supply at these sites pose challenges to effectively delivering insoluble drugs in micelles. Incorporating targeting ligands on the surface of drug carriers can enhance drug delivery efficiency[24,25]. Magainin, a small antimicrobial peptide found in the skin of *Xenopus* frogs, has demonstrated activity against a wide range of gram-positive and gram-negative bacteria. Magainin II (MagII), a member of the Magainin family, is particularly effective. Modifying the micellar surface with MagII improves its active targeting capability, enabling more efficient drug delivery to the site of bacterial infection sites and enhancing therapeutic outcomes[26,27].

In this study, we developed micelles composed of the microenvironment-responsive polymer PDPA and the amphiphilic polymer D-α-Tocopherol Polyethylene Glycol 1000 Succinate ($TPGS_{1000}$). These micelles were used to encapsulate AZI and Cur and further functionalized with DSPE-PEG_{2000}-MagII on their surface. Because of its ability to recognize and destroy bacteria in numerous host cells, MagII enables micelles to actively target bacterial infection sites at various depths after entering the systemic circulation. When the micelles are actively targeted to the infection site, the PDPA component responds to the slightly acidic microenvironment, triggering the release and accumulation of the therapeutic agents AZI and Cur, thereby enhancing their therapeutic effects. This study evaluated the therapeutic efficacy of these environment-responsive targeted micelles against infections at different depths. The findings have significant implications for the treatment of drug-resistant bacterial infections.

Results

Investigation of synergistic effect

The collaboration index was calculated based on the Bliss independent model[28,29]. According to the calculation formula of the Bliss model, the combined effect is the sum of the individual effects of the two inhibitors on the growth rate. We examined the combined effect of AZI and Cur, and the results were shown in Table S1. The results showed that the maximum synergy index between 12.5 μM AZI and 25 μM Cur was 0.53.

Characterization of micelles

After confirming the synergistic antibacterial effect of AZI and Cur, we constructed an environmentally responsive MagII-modified AZI and Cur micelles (MagII-AZI/Cur-Ms). The morphology of MagII-AZI/Cur-Ms was observed using TEM, and the result is shown in Fig. 1A. The figure shows that the micelles appeared spherical or quasi-spherical with uniform sizes. The encapsulation efficiency (EE) of AZI and Cur among MagII-AZI/Cur-Ms was 91.66% ± 0.78% and 83.65% ± 1.43%, respectively. The particle size distribution and potential distribution of MagII-AZI/Cur-Ms are shown in Fig. 1B,C. The research results indicate that the micelles had a negative Zeta potential. The particle sizes of different formulations were between 20 and 30 nm, and the polydispersity index (PDI) values were less than 0.22. The particle size of the MagII-AZI/Cur-Ms was 36.19 ± 1.46 nm, and the zeta potential was − 1.27 ± 0.15 mV. The particle size and potential of micelles were measured at pH 6.5 to investigate the state of targeted micelles in a slightly acidic environment simulating bacterial infection. As shown in Fig. 1D,F, the particle size of MagII-AZI/Cur-Ms was 127.38 ± 2.02 nm, the zeta potential was − 2.9 ± 0.26 mV, and the PDI values were less than 0.24 at pH 6.5. Figure 1G shows the relationship between pyrene's I_{373}/I_{384} absorption ratio and micelle mass concentration. It indicated that the critical micelle concentration (CMC) value of MagII-AZI/Cur-Ms was 0.0178 mg/mL. Figure 1H,I shows the evaluation results of micelle stability. After 0 days, the EE of AZI was about 90%, and the EE of Cur was about 85%. The EE of both drugs decreased with the passage of storage time, and the decrease at 4 °C was slower than that at 25 °C. On day 20, the EE of AZI at 4 °C and 25 °C was 72.01% ± 1.32% and 58.69% ± 1.03%, respectively. The EE of the Cur at 4 °C and 25 °C was 70.46% ± 0.79% and 54.60% ± 2.24%, respectively.

Colocalization of fluorescently labeled micelles and planktonic bacteria.

Figure 2 shows the qualitative and quantitative analyses of Colocalization of Fluorescently Labeled Micelles and Planktonic Bacteria. We used the fluorescent probe Cou to label the micelles and co-localized them with planktonic bacteria to evaluate the targeting capability of the micelles. The particle size of Cou-Ms was 32.71 ± 1.15 nm, PDI was 16.24 ± 6.09%, and Zeta potential was − 2.2 ± 0.62 mV. The particle size of MagII-Cou-Ms was 36.50 ± 4.08 nm, PDI was 17.59 ± 2.34%, and Zeta potential was − 2.33 ± 0.42 mV. Cou-Ms and MagII-Cou-Ms have similar particle sizes to the drug-loaded micelles, both have a negative Zeta potential and a relatively narrow PDI (Fig. S1). Figure 2A shows the co-localization of planktonic bacteria with micelles under an inverted fluorescence microscope. The fluorescence density was analyzed using Image J, and the results are shown in Fig. 2B. Combining the results of these two experiments, we found that the amounts of Coumarin (Cou) absorbed by cells in each group were in the order: MagII-modified Cou micelles (MagII-Cou-Ms) > Coumarin micelles (Cou-Ms).

Evaluation of antibacterial activity in vitro

First, the minimum inhibitory concentration (MIC) of each formulation was determined by the microbroth dilution method. The AZI concentration in AZI micelles (AZI-Ms), AZI plus Cur micelles (AZI/Cur-Ms), and MagII-AZI/Cur-Ms groups was 2.5, 1.25, and 0.625 μM when the bacterial fluid in the plate showed a clear state. As shown in Supplementary Table S2, the MIC of MagII-AZI/Cur-Ms against MRSA was determined to be 0.625 μM. Blank micelles had no antibacterial activity, and when both AZI and Cur were encapsulated in the micelles, the MIC was lower than that when AZI was encapsulated separately. The growth of bacteria after treatment was dynamically monitored, and the time–growth curve of bacteria after administration was plotted. Figure 3A

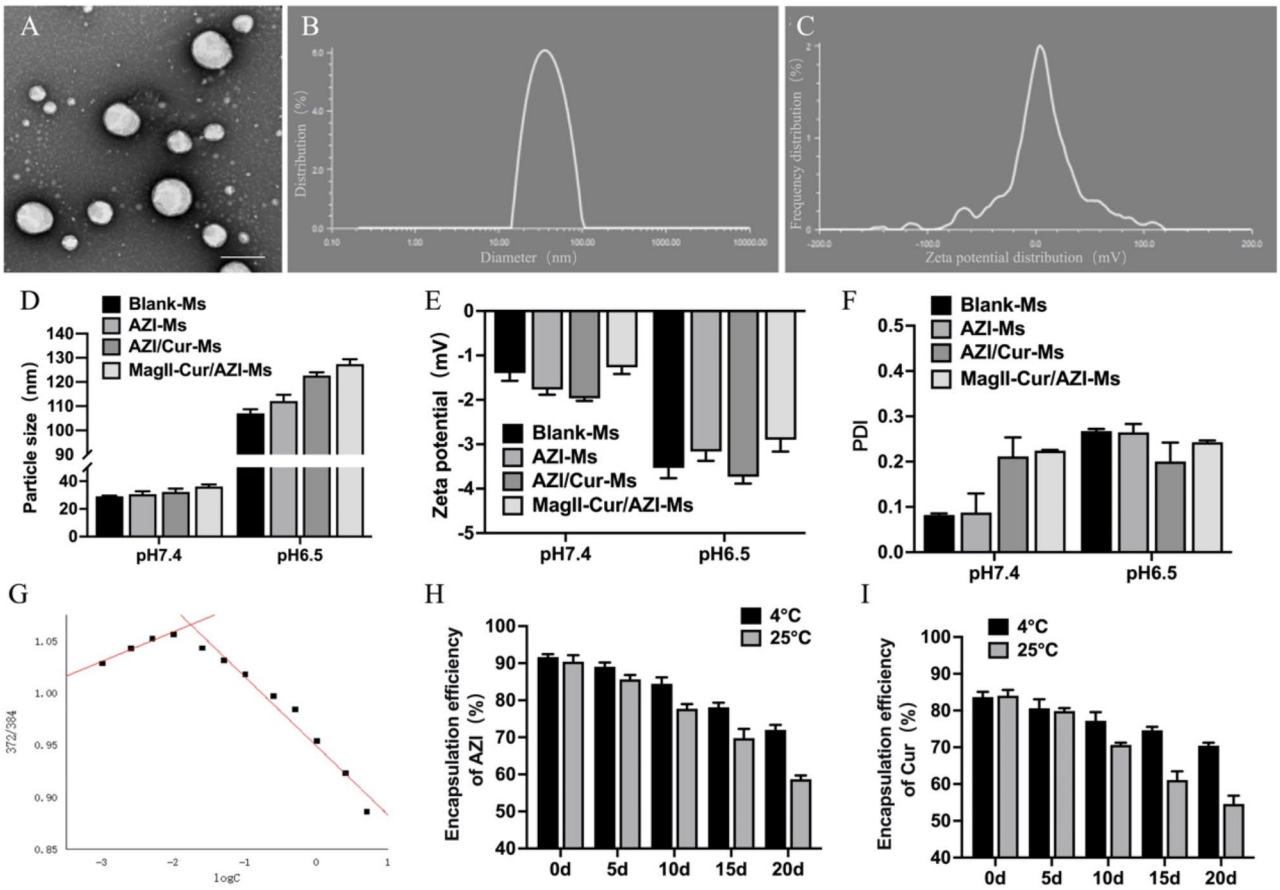

Fig. 1. Characterization of MagII-AZI/Cur-Ms. (**A**) TEM image of MagII-AZI/Cur-Ms. Scale bar, 20 nm. (**B**) Particle size distribution map of MagII-AZI/Cur-Ms. (**C**) Zeta potential distribution map of MagII-AZI/Cur-Ms. (**D**) Particle size of different formulation at pH7.4 and pH6.5. (**E**) Zeta potential of different formulation at pH7.4 and pH6.5. (**F**) PDI of different formulation at pH7.4 and pH6.5. (**G**) Determination of CMC. (**H**) EE of AZI at different times under 4 °C and 25 °C conditions. (**I**) EE of Cur at different times under 4 °C and 25 °C conditions. Data are presented as mean ± SD ($n = 3$), $P < 0.05$.

shows the time-growth curves of bacteria under different micelles in the four compound pores. We combine this into Fig. 3B. It was observed that the control group entered a stable growth state. In contrast, the AZI-Ms, AZI/Cur-Ms, and MagII-AZI/Cur-Ms groups showed different degrees of growth inhibition after 4 h. The growth rates of bacteria in AZI-Ms, AZI/Cur-Ms, and MagII-AZI/Cur-Ms groups slowed down and were the lowest in the MagII-AZI/Cur-Ms group. These results indicated that MagII-AZI/Cur-Ms had a significant inhibitory effect on the growth and reproduction of MRSA.

The antibacterial zone size of drug-carrying micelles was tested, and the results are shown in Fig. 3C,D. The diameters of the inhibition zones for the AZI-Ms and AZI/Cur-Ms groups were 16.85 ± 0.79 μm and 18.23 ± 0.62 μm, respectively. The diameter of the antibacterial zone in the MagII-AZI/Cur-Ms group increased to 20.89 ± 1.60 μm with the addition of Cur and modification of MagII. The scanning electron microscope (SEM) results showed that the morphology of MRSA treated with Blank-Ms was complete, and the body was smooth. After treatment with different formulations, the intracellular bacterial content leaked (Fig. 3E), with the MagII-AZI/Cur-Ms group showing significant morphological changes.

Destructive effect of MagII-AZI/Cur-Ms on biofilms

In this study, the effects of MagII-AZI/Cur-Ms on MRSA biofilms were investigated by crystal violet staining and live/dead bacterial staining. Different formulations exhibited inhibitory effects on biofilms, with the MagII-AZI/Cur-Ms group showing the most obvious inhibitory effect (Fig. 4B). Live/Dead bacterial staining was used to stain the cells in the biofilm to further verify this finding. The 3D results of live/dead bacterial staining are shown in Fig. 4A. The number of live cells decreased, whereas the number of dead cells increased successively in the order of Blank-Ms, AZI-Ms, AZI/Cur-Ms, and MagII-AZI/Cur-Ms groups.

ROS measurement

We treated different groups of planktonic bacteria with 2′,7′-DCFH-DA to further explore the mechanism of micellar destruction of bacteria. The MagII-AZI/Cur-Ms group showed the most significant increase in Reactive

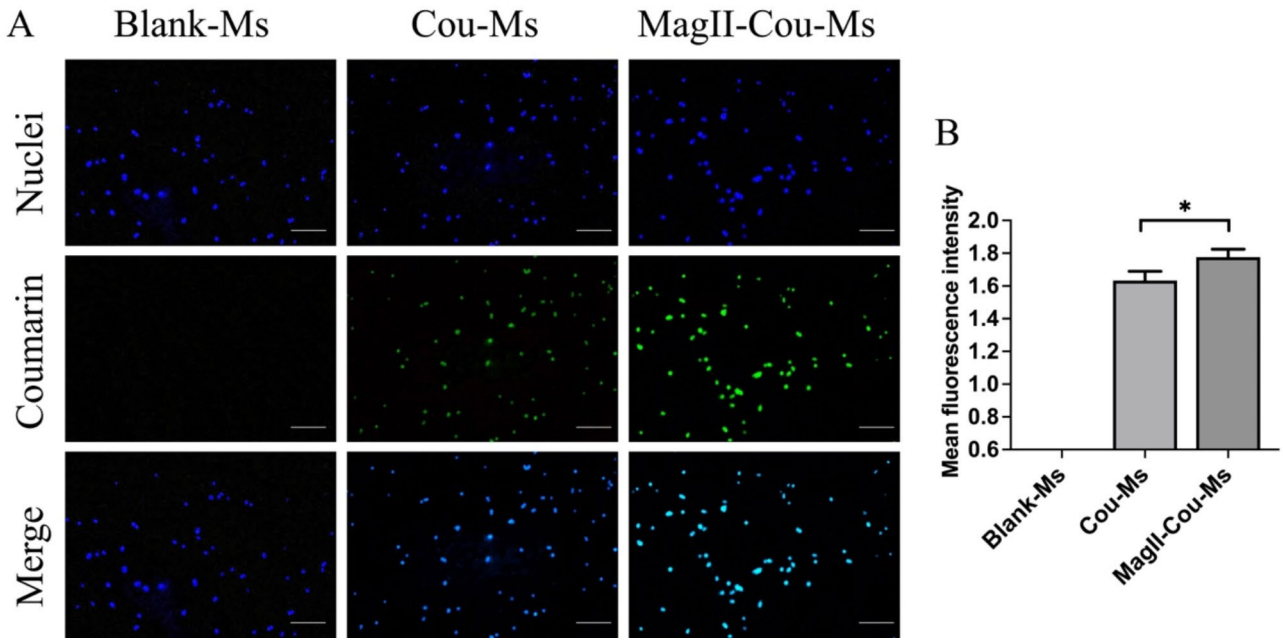

Fig. 2. Targeting effects after incubation with varying formulations. (**A**) Co-localization of planktonic bacteria with fluorescently labeled micelles. Scale bar = 50 μm. (**B**) Quantitative analysis of fluorescence intensity. Scale bar, 25 μm. Data are presented as mean ± SD ($n = 3$), $^{*}P < 0.05$.

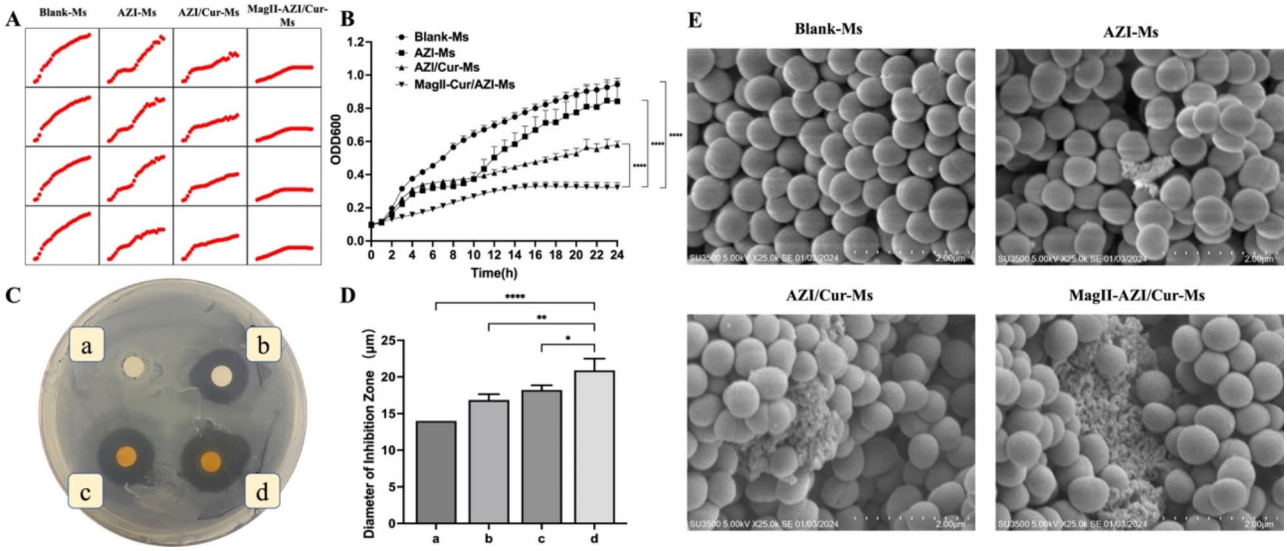

Fig. 3. Evaluation of antibacterial activity *in vitro*. (**A**) The time–growth curve of different micelles. (**B**) Summary of time–growth curve. (**C**) Representative image of bacteriostatic zone. a, for Blank-Ms. b, for AZI-Ms. c, for AZI/Cur-Ms. d, for MagII-AZI/Cur-Ms. (**D**) Quantitative analysis of bacteriostatic zone. a, for Blank-Ms. b, for AZI-Ms. c, for AZI/Cur-Ms. d, for MagII-AZI/Cur-Ms. (**E**) Representative images of bacteria by SEM after treatment with different formulations. Data are presented as mean ± SD ($n = 3$), $^{*}P < 0.05$. $^{**}P < 0.01$, $^{****}P < 0.005$.

oxygen species (ROS) compared with the Blank-Ms and AZI-Ms groups (Fig. 4C). However, there was no significant difference in ROS increase between the AZI/Cur-Ms group and the MagII-AZI/Cur-Ms group.

In vivo fluorescence imaging

A noninvasive optical imaging system was used to capture the real-time images of model mice to evaluate the targeting of micelles. Since neither AZI nor Cur fluoresces, we chose lipophilic fluorescent dye DiR instead of AZI and Cur to investigate the distribution of micelles in animals. The particle size of DiR-Ms was

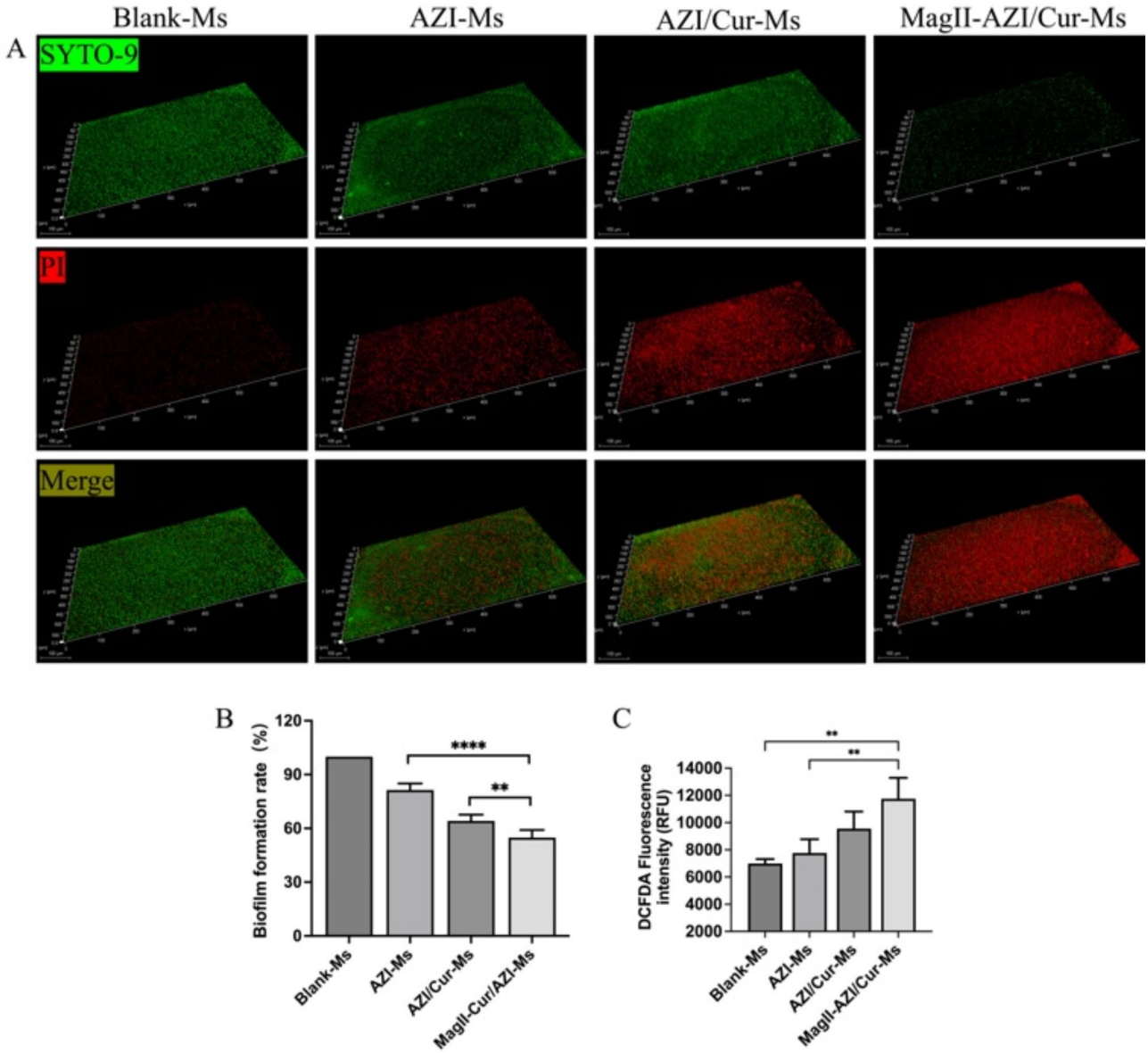

Fig. 4. Inhibition of biofilms. (**A**) Results of living/dead bacteria staining in biofilm. (**B**) Results of quantitative analysis of crystal violet staining. (**C**) ROS measurement. Data are presented as mean ± SD, $^{*}P < 0.05$, $^{**}P < 0.01$, $^{****}P < 0.005$.

35.73 ± 4.64 nm, PDI was 17.73 ± 7.85%, and zeta potential was − 2.2 ± 1.44 mV. The particle size of MagII-DiR-Ms was 38.13 ± 6.63 nm, PDI was 16.36 ± 6.19%, and zeta potential was − 2.07 ± 1.27 mV. MagII-DiR-Ms and DiR-Ms have similar particle sizes to those of encapsulated AZI and Cur micelles, both carry a negative Zeta potential, and have a relatively narrow PDI (Fig. S2). In vivo imaging of the three different depth models of bacterial infection showed that only a small fraction of the free DiR accumulates at the site of bacterial infection. The MagII-modified DiR micelles (MagII-DiR-Ms) could accumulate at the infected site for 96 h, and the DiR concentration at the infected site was higher than that of the unmodified DiR micelles (DiR-Ms) (Figs. 5 and 8A and S8).

Evaluation of pharmacodynamics in vivo

The antibacterial effect was investigated in skin infection, muscle infection, and pneumonia models with different depths of bacterial infection to further verify the effect of MagII-AZI/Cur-Ms in vivo. First, the therapeutic effect of micelles on superficial infection was investigated. Figure 6A shows the representative images of the skin infection wound on day 6 of treatment. All mice with skin infections showed some degree of suppuration on day 1. The wounds were scabbed after 4 days of suppuration in the saline group, and redness and swelling were observed around the scabbed part on day 6. The redness and swelling disappeared, and large scabs appeared in the free AZI and Cur (free AZI/Cur) groups. The scab faded and returned to a near-healthy state in the MagII-

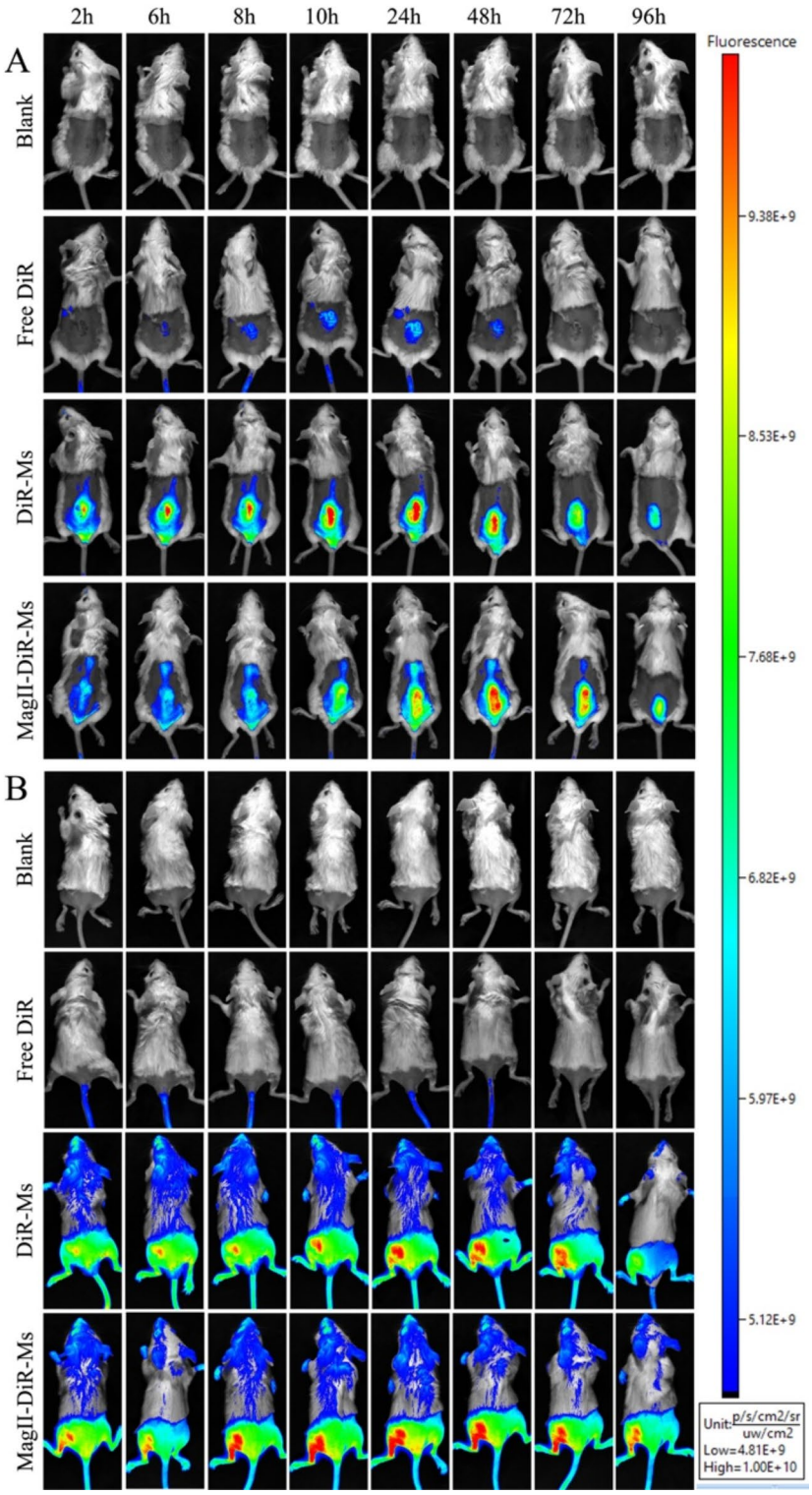

Fig. 5. Real-time imaging observation of mice treated with varying formulations in vivo. (**A**) Representative real-time imaging results of skin infection mice. (**B**) Representative real-time imaging results of muscle infection mice.

AZI/Cur-Ms group. Figure 6B shows the representative image of mice with muscle infection on day 6 after treatment. All mice with muscle infection showed redness and swelling of leg muscles, inability to bend joints, and limited movement on day 1. The symptoms of mice in the saline group and free AZI/Cur groups were not relieved after treatment. The mice in the AZI/Cur-Ms group experienced mild remission, whereas the muscle redness disappeared in the MagII-AZI/Cur-Ms group, and the mouse activity returned to normal. The infected

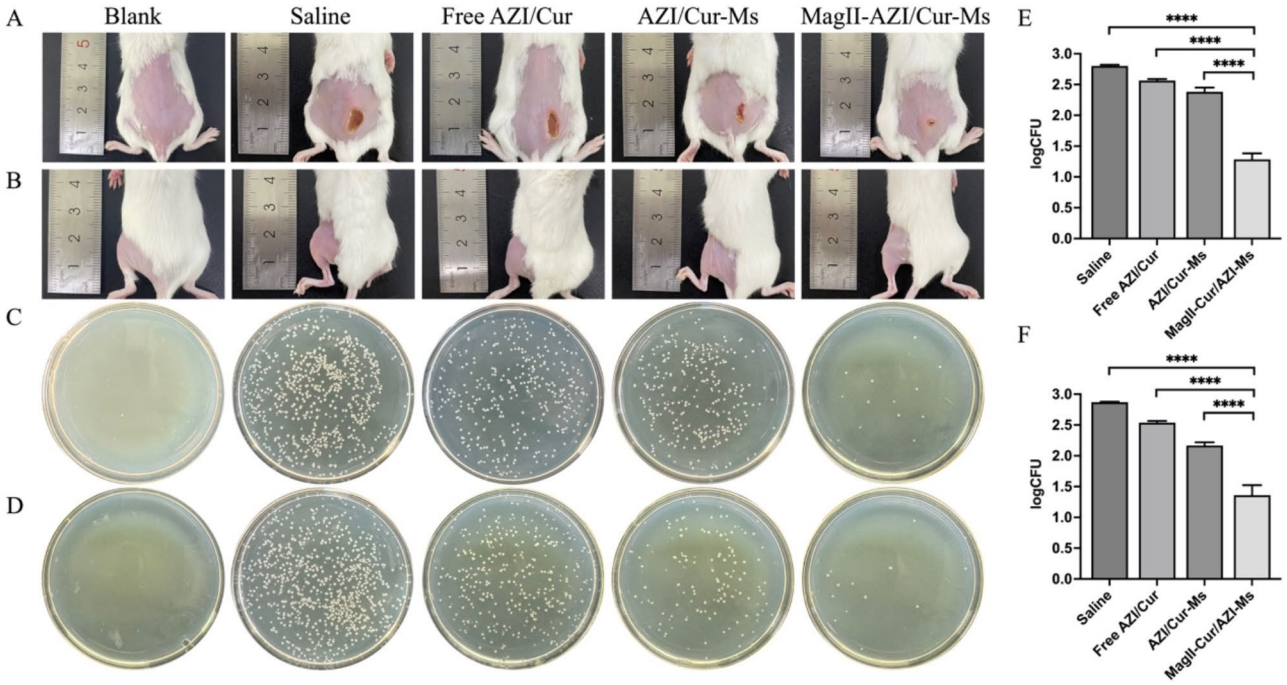

Fig. 6. Representative images of mice with skin infection and muscle infection and bacterial count at infection site. (**A**) Representative images of mice with skin infection after treatment. (**B**) Representative images of mice with muscle infection after treatment. (**C**) Representative images of skin tissue homogenate plate spreading. (**D**) Representative images of muscle tissue homogenate plate spreading. (**E**) Quantitative analysis of bacterial colony number in skin infection site. (**F**) Quantitative analysis of bacterial colony number in muscle infection site. Data are presented as mean ± SD ($n = 6$), $^{*}P < 0.05$, $^{**}P < 0.01$, $^{****}P < 0.005$.

sites of mice with skin and muscle infections were homogenized and cultured on an LB solid medium, as shown in Fig. 6C,D. The bacterial growth of skin and muscle infected mouse tissues is shown in Fig. S4A,B. The MagII-AZI/Cur-Ms group had the lowest number of bacteria in the skin and muscle infected mice (Fig. 6E,F). It showed that MagII-AZI/Cur-Ms can effectively treat bacterial infections.

Tissue samples from the infection sites of mice in each model group were collected for HE and Masson staining to assess inflammation, necrosis, and inflammatory cell infiltration after treatment (Fig. 7A–D). HE staining revealed normal skin morphology and structure in the blank group, with no significant inflammatory reactions in epithelial cells. Compared with the saline group, the MagII-AZI/Cur-Ms-treated group exhibited more intact epithelial cells. Masson staining showed substantial collagen deposition in the skin tissue of the MagII-AZI/Cur-Ms group. In contrast, the saline and free AZI/Cur groups exhibited disordered and loosely distributed muscle structures with evident abscess formation. After MagII-AZI/Cur-Ms treatment, the muscle tissue became organized, significantly reducing pathological damage from bacterial infections. Masson staining showed that the number of intercellular collagen fibers was notably lower in the treatment group than in the model group, with the least collagen observed in the MagII-AZI/Cur-Ms group. These results indicated that MagII-AZI/Cur-Ms effectively inhibited inflammation at infection sites. The serum levels of tumor necrosis factor TNF-α, interleukin IL-1β, and IL-6 were measured in mice with skin infection (Fig. 7E–G) and muscle infection (Fig. 7H–J). The levels were significantly lower after MagII-AZI/Cur-Ms treatment than those in the saline and free AZI/Cur groups and even lower than in the AZI/Cur-Ms group.

Finally, a pneumonia model was established to treat deep bacterial infections. In vitro imaging results of the lungs are shown in Fig. 8A. Post-treatment, the lungs of mice with pneumonia were homogenized in pre-cooled PBS and plated on LB solid medium. The results showed that MagII-AZI/Cur-Ms effectively inhibited bacterial growth at the infection site (Figs. 8B and S4C). HE staining of lung tissue (Fig. 8C) revealed normal lung structure with no congestion, edema, or inflammatory exudation in the blank group. Lung hyperemia and inflammatory cell infiltration were pronounced in the saline group. Hyperemia and inflammatory cell infiltration were improved to varying degrees in the free AZI/Cur, AZI/Cur-Ms, and MagII-AZI/Cur-Ms groups, with the most significant improvement observed in the MagII-AZI/Cur-Ms group.

Immunofluorescence staining revealed increased expression of C5aR1, C5b-9, C3c, and NF-κB p65 in the saline group, indicating complement system activation. Treatment with MagII-AZI/Cur-Ms significantly reduced expression (Fig. 8D,G). The results of semi-quantitative immunofluorescence analysis are shown in Fig S5. In addition, bronchoalveolar lavage fluid (BALF) analysis revealed reduced levels of TNF-α, IL-1β, and IL-6 in the MagII-AZI/Cur-Ms group compared with the saline group, indicating almost complete elimination of lung inflammation (Fig. 8H,J). Reye's staining showed that the white blood cells (WBCs), Neu, and Lym

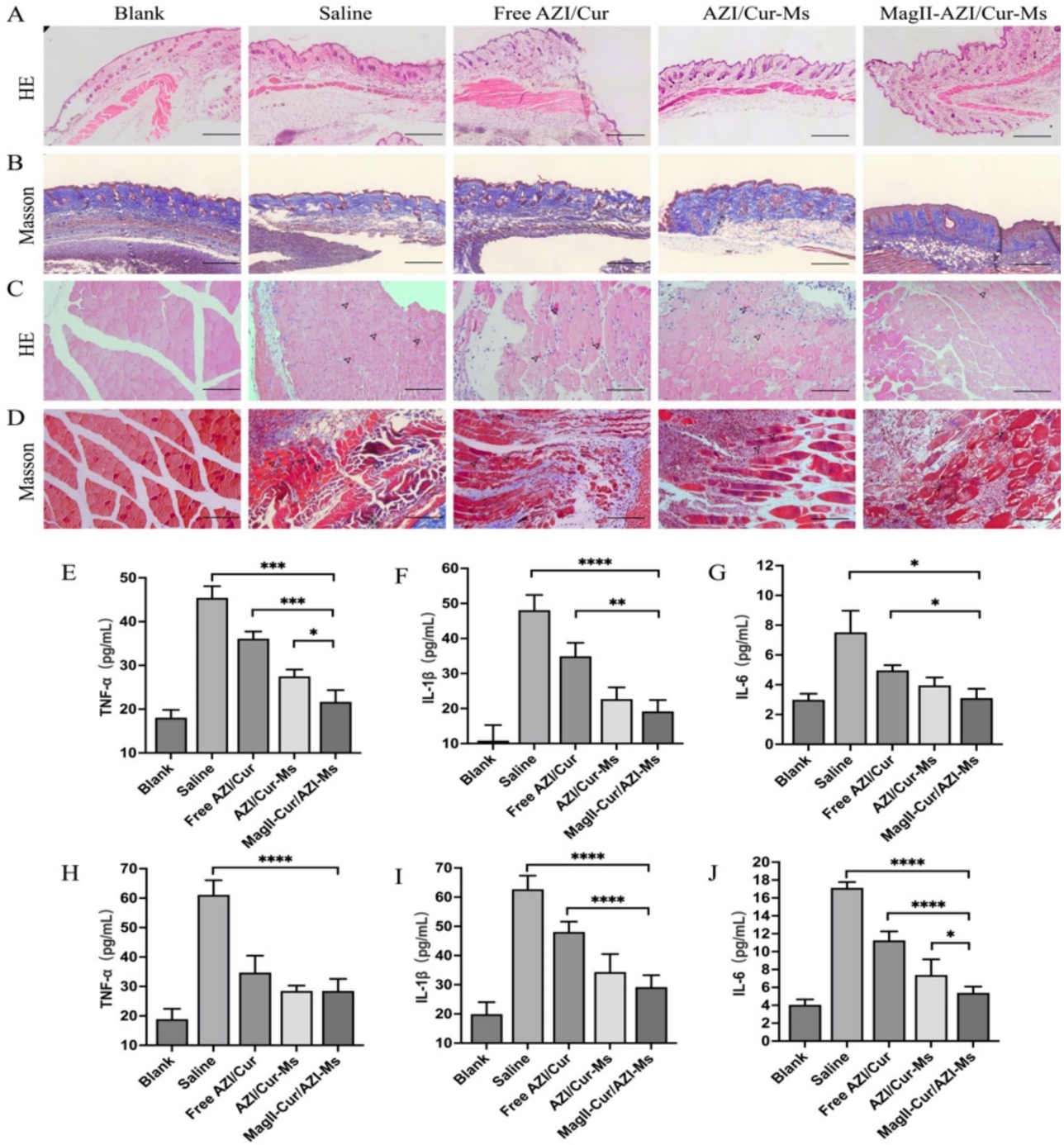

Fig. 7. Antibacterial effect of different micellar preparations after treatment. (**A**) Representative images of pathological changes in skin tissue by HE staining. (**B**) Representative images of pathological changes in skin tissue by Masson staining. (**C**) Representative images of pathological changes in muscle tissue by HE staining. (**D**) Representative images of pathological changes in muscle tissue by Masson staining. (**E**–**G**) Expression of inflammatory factors in blood of mice with skin infection after treatment with different formulations. (**H**–**J**) Expression of inflammatory factors in blood of mice with muscle infection after treatment with different formulations. Scale bar = 50 μm. Data are presented as mean ± SD ($n = 6$), $^{*}P < 0.05$, $^{**}P < 0.01$, $^{****}P < 0.005$.

counts in the MagII-AZI/Cur-Ms group approached healthy levels (Fig. 8K,M). These findings demonstrated the targeted antibacterial efficacy and therapeutic potential of MagII-AZI/Cur-Ms in lung infections.

Safety evaluation

The results of the safety evaluation are presented in Supplementary Fig. S5. HE staining showed no significant organ damage in any group following treatment with micelle preparations (Fig. S6A). The mouse body weight

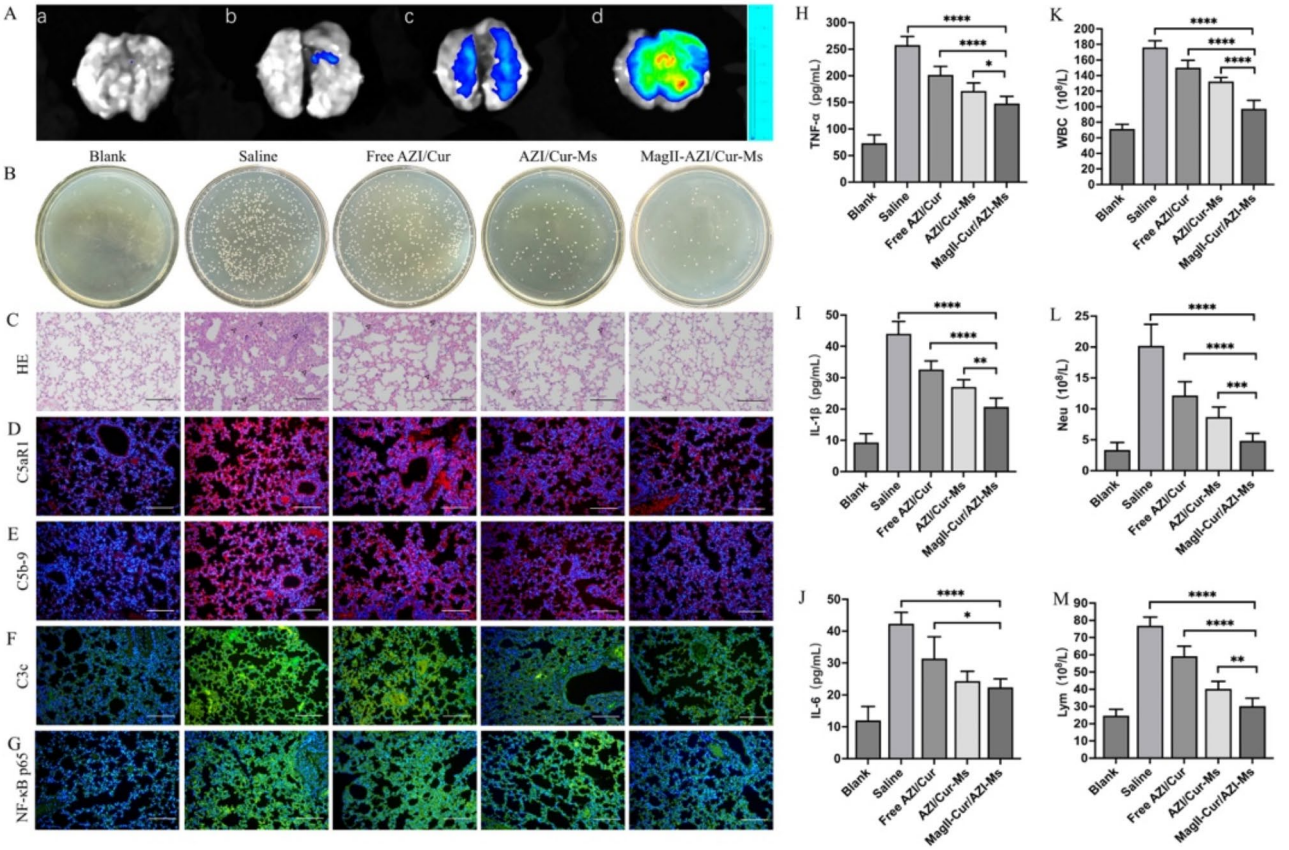

Fig. 8. Antibacterial effect of different micellar preparations on mice with pneumonia. (**A**) Real-time imaging observation of lungs treated with varying formulations in vivo. a, for Blank-Ms. B, for free DiR. c, for DiR-Ms. d, for MagII-DiR-Ms. (**B**) Representative images of lung tissue homogenate plate spreading. (**C**) Representative images of pathological changes in lungs by HE staining. (**D**–**G**) Expression of C5aR1, C5b-9, C3c and NF-κB p65 detected by immunohistochemistry in lungs. (**H**–**J**) Expression of inflammatory factors in BALF after treatment with different formulations. (**K**–**M**) Number of inflammatory cells in BALF after treatment with different micelles. Scale bar = 50 μm. Data are presented as mean ± SD ($n = 6$), $^{*}P < 0.05$, $^{**}P < 0.01$, $^{****}P < 0.005$.

remained stable throughout treatment (Fig. S6B). Blood analysis revealed no significant changes in WBC, granulocyte (GRA), or Lym counts after treatment (Supplementary Fig. S6C–E), indicating high biocompatibility. The hemolysis test revealed a hemolysis rate of 4.81% ± 0.70% for MagII-AZI/Cur-Ms, demonstrating good biosafety (Supplementary Fig. S6F). The long-circulation test showed that micelles extended blood circulation time compared with free DiR, with DSPE-PEG_{2000}-MagII modification further enhancing this effect (Supplementary Fig. S6G).

Discussion

The resistance of pathogenic bacteria has significantly increased in recent years due to the excessive or improper use of antibiotics, making antimicrobial resistance one of the most critical public health threats globally. Among these bacteria, *Staphylococcus aureus* is particularly deadly, causing infections at various depths in the body[1,2]. Developing new antibacterial drugs or materials is urgently needed to manage bacterial infections. AZI, a commonly used clinical antibiotic in current clinical practice, faces the challenges of increasing toxicity at higher therapeutic doses. To address this issue, researchers combined AZI with Cur, which is known for its anti-inflammatory and anti-infective properties, to reduce dosage while maintaining therapeutic efficacy[12,14,15]. However, both AZI and Cur exhibited limitations such as poor water solubility, low bioavailability, and instability[18]. These challenges were addressed by constructing an acid-responsive polymer micelle that encapsulates AZI and Cur, allowing for targeted delivery to the slightly acidic microenvironment of bacterial infection[20].

The delivery of insoluble drugs using micelles is particularly challenging due to the variations in vascular density and blood supply across different infection depths. MagII, a small antimicrobial peptide, was added to the micellar surface to enhance targeting, improving its ability to actively target bacterial infection sites[26]. The MagII-AZI/Cur-Ms micelles were successfully constructed and characterized. The probabilistic theory states that the combined effect of two inhibitors on survival is defined as the probability of being affected by at least one of the inhibitors. Based on this theory, the Bliss model was developed, which equates Bliss independence to the sum of all individual effects of various inhibitors[30]. When applied to the specific case of bacterial growth rates,

the combined effect is the sum of the individual effects of the two inhibitors on the growth rate. Therefore, the maximum achievable effect with two inhibitors is predicted according to Bliss independence. A synergy index greater than "0" indicates that the two drugs have a synergistic effect. The closer the value is to "1," the stronger the synergistic effect. AZI and Cur show a strong effect, confirming their combined antibacterial efficacy.

Particle size is an essential factor influencing the EE, stability, and other physicochemical properties of targeted preparations. After MagII modification, the particle size and zeta potential of AZI/Cur-Ms slightly increased, possibly due to the positive charge of MagII[26]. The particle size distribution of MagII-AZI/Cur-Ms followed normal characteristics with a narrow polydispersion coefficient. Although the zeta potential was just below 0 mV and slightly negative, the hydration layer on the outer layer of the micelle maintained stability and facilitated prolonged circulation in the body. The micelles exhibited significant changes in particle size and zeta potential in a slightly acidic environment mimicking bacterial infections, confirming the pH-responsive behavior of PDPA, which altered micelle structure. CMC is the lowest concentration of surfactant molecules associated with the formation of micelles in solution[31,32]. The surface tension of the solution is no longer reduced, and a large number of micelles are formed when the solution concentration is greater than CMC. Small CMC values enable MagII-AZI/Cur-Ms to maintain structural integrity. Due to the flocculation of micelles and the leakage of drugs during placement, the EE of micelles decreased within 20 days. Stability tests revealed minimal leakage of AZI and Cur in 20 days, with EE remaining above 50%, thus confirming the stability of MagII-AZI/Cur-Ms.

We investigated the targeting ability of environment-responsive micelles, specifically MagII-Cou-Ms, toward planktonic MRSA after successfully constructing environment-responsive MagII-AZI/Cur-Ms. As neither AZI nor Cur exhibits fluorescence, Cou with fluorescence was selected as a fluorescence probe to investigate the targeting of micelles to bacteria by fluorescence microscopy[33]. The results indicated that the targeting ability of micelles modified by MagII was significantly enhanced. MagII, an antimicrobial peptide, is known to interact with bacterial membranes by forming α-helix structures, which enable it to induce membrane disruption and facilitate the transmembrane transfer of peptides. This property allows MagII to effectively target and damage microbial cell walls while minimizing damage to human host cells. The enhanced targeting observed in MagII-modified micelles may be due to this specific interaction, which enhances the affinity of the micelles for MRSA and facilitates their entry into bacterial[34,35].

The antibacterial effects of different micelle formulations were evaluated in vitro. AZI and Cur have poor water solubility, which makes it difficult for them to be evenly distributed in the culture medium in vitro experiments, thereby affecting the drug efficacy. Therefore, we examined the MIC of different micelles. Studies have shown that the MIC of AZI against MRSA was 2 μg/mL[36]. In this study, the MIC of AZI-Ms was slightly higher than this value. This is due to the strong hydrophobic interaction between the drug and the micelle core, resulting in a slower release rate of the drug encapsulated in the micelles, which in turn leads to less significant inhibitory effects compared to free drugs. In addition, the good stability of the micelles also contributed to this result. When used alone, the MIC of Cur is 125 to 500 μg/mL[37]. However, when combined with AZI, the addition of Cur reduced the MIC of AZI-Ms, indicating a good synergistic effect between AZI and Cur. After modification with DSPE-PEG_{2000}-MagII, the MIC of AZI/Cur-Ms was further reduced, confirming the targeting ability of DSPE-PEG_{2000}-MagII. The bacteriostatic zone experiment is a common method used to test the titer of antibiotics. The concentration difference of antibiotics from high to low is formed after the diffusion of antibiotics on the solid LB medium. The bacteria on the medium do not reproduce when the antibiotic concentration on the edge reaches the MIC, thus producing a certain size of inhibitory zone to test the antibacterial activity of antibiotics[38,39]. The result of the bacteriostatic zone experiment also indicated the bacteriostatic effect of MagII-AZI/Cur-Ms. In addition, the bacteriostatic effect of MagII-AZI/Cur-Ms was directly observed through the morphological changes of bacteria.

We further investigated the bacteriostatic mechanism of MagII-AZI/Cur-Ms. Bacteria rely on their own synthesis of proteins, polysaccharides, extracellular DNA (eDNA), and other non-water-soluble extracellular polymeric substances that cross-link to form dense biofilms after adhering and colonizing to biological or abiotic surfaces[40–42]. Biofilms exhibit strong hydrophobicity, which prevents the penetration of antibiotics and the infiltration of immune cells through electrostatic adsorption and physical shielding. Biofilms act as a natural physical barrier, contributing to bacterial drug resistance. In addition, biofilms can induce bacterial metabolic quiescence, stress responses, and quorum sensing or upregulate the expression levels of the bacterial efflux pump expression levels, further increasing drug resistance[43,44]. As a result, bacterial biofilms can colonize the human body for extended periods, leading to local inflammation, chronic infections, and severe outcomes such as sepsis, organ failure, or death[45–47].

Crystal violet staining is a commonly used method for detecting biofilms due to its simplicity, convenience, and relative accuracy, allowing for the semi-quantitative analysis of total biofilm[48]. SYTO-9, a green fluorescent nucleic acid dye, penetrates intact cell membranes to label live bacteria, whereas PI only stains bacteria with intact damaged membranes[49]. The results demonstrated that MagII-AZI/Cur-Ms effectively disrupted biofilm formation.

DCFH-DA can be oxidized by cytoplasmic ROS to produce a strongly green fluorescent compound, 2′,7′-dichlorofluorescein (DCF), which is used to quantify ROS formation. Studies suggest that the body generates some ROS to combat bacterial infections. Excessive ROS production can enhance the antibacterial effect against drug-resistant bacteria, prevent biofilm formation, and destroy existing biofilms[50–52]. Based on the inhibitory effect of MagII-AZI/Cur-Ms on bacterial growth and biofilm destruction, we preliminatively concluded that the antibacterial activity of MagII-AZI/Cur-Ms is partly related to ROS induction.

After confirming the potent antibacterial activity of MagII-AZI/Cur-Ms in vitro, we examined its efficacy in vivo. Three bacterial infection models—skin infection, muscle infection, and lung infection—were constructed to simulate varying infection depths and assess the therapeutic effects of the drug under these conditions. Studies indicate that enhanced permeability and retention (EPR) effects, similar to those observed in tumors, occur at

bacterial infection sites. This facilitates the accumulation of nanoparticles at the infection site through passive targeted transport[53–55]. In this study, micelles modified with MagII demonstrated strong targeting properties, possibly due to their small particle size. This enhanced passive targeting to bacterial infection sites via the EPR effect, increasing drug accumulation. The DSPE-PEG_{2000} in the micelles formed a hydrophilic membrane on the micelle surface, improving hydrophilicity and prolonging the drug's circulation time in the body. Additionally, modifying antimicrobial peptide MagII enabled micelles to actively target bacterial infection sites, further enhancing drug accumulation at the infection site.

The in vivo antibacterial effects of MagII-AZI/Cur-Ms were evaluated using skin, muscle, and pneumonia models with bacterial infections at varying depths. Based on HE staining, Masson staining, bacterial plating, and inflammatory cytokine expression analysis, MagII-AZI/Cur-Ms demonstrated significant therapeutic effects in treating skin and muscle infections. This was attributed to the inhibitory effect of micelles on the inflammatory response at the site of bacterial infection. After treatment, the pathological injury of muscle tissue was weakened, accompanied by a decrease in the number of collagen fibers. The results suggest that micelles promote muscle tissue repair and regeneration, allowing damaged tissue to reorganize, thereby reducing the inflammatory response caused by bacterial infection and the deposition of collagen fibers. In addition, during normal tissue repair, collagen fibers undergo degradation and remodeling to restore the normal structure and function of the tissue[56,57]. The degradation and remodeling process of collagen fibers explains the decrease in the number of collagen fibers after treatment.

We evaluated the efficacy of MagII-AZI/Cur-Ms in a pulmonary bacterial infection model to explore the therapeutic potential of micelles in treating deep-organ bacterial infection. Similarly, MagII-AZI/Cur-Ms have a good effect on the treatment of bacterial infections in the lungs. The complement system is the first line of defense against microbial invasion. Overactivation of the complement system is a recognized mechanism of bacterial pneumonia. Complement components C3 and C5 are particularly implicated, enhancing inflammation and activating macrophages. Furthermore, the C5a receptor triggers cytokine storms characterized by elevated levels of IL-6 and TNF-α, which can amplify cell sensitivity to infections[58–60]. MagII-AZI/Cur-Ms effectively inhibited complement system activation in the lungs and suppressing the overproduction of inflammatory cytokines. This regulation highlights their potential in addressing bacterial infections and the associated inflammatory complications. Safety evaluations of organ tissues and blood samples confirmed that the micelles exhibited low toxicity, long circulation times, and no adverse effects, supporting their suitability as a therapeutic strategy for pulmonary bacterial infections.

Recent studies have shown that compared to free antibiotics, antibiotics encapsulated in micelles can more effectively kill bacteria and inhibit the formation of bacterial biofilms within the same time[61]. Additionally, research has confirmed the excellent therapeutic effects of combining azithromycin and curcumin in nano emulsions[62]. Some studies have focused on using antimicrobial peptide-modified micelles to treat infections caused by MRSA[63]. This study extends the application to infection models of different depths, such as skin, muscle, and lung. In this study, we conducted a more comprehensive evaluation of the micelles in infection models of varying depths, providing more data to support their application at different infection sites. In addition, we introduced the combination of targeting ligands and environmentally responsive materials, which synergistically enhances antibacterial efficacy and reduces bacterial resistance through multiple mechanisms, offering new insights for the treatment of MRSA.

Materials and reagents

$TPGS_{1000}$, AZI and Cur were obtained from Meilun Co., Ltd. (Dalian, China). Polyethylene glycol-distearoyl phosphatidylethanolamine (DSPE-PEG_{2000}) was purchased from NOF Co., Ltd. (Tokyo, Japan). DSPE-PEG_{2000}-MagII and $mPEG_{114}$-$PDPA_{10}$ were synthesized and provided by Xian Ruixi Biological Technology Co., Ltd. (Xian, China). 3,3,3,3-tetramethylindotricarbocyanineiodide (DiR) was obtained from Sigma (Sigma-Aldrich). ELISA kit, live/dead bacterial viability kit and Luria-Bertani (LB) culture were purchased from Beijing Solarbio Technology Co., Ltd. (Beijing, China). C5aR1 and NF-κB p65 antibodies were purchased from Boster Co., Ltd. (Wuhan, China). C5b-9 antibodies were purchased from Bioss Co., Ltd. (Beijing, China). C3c antibodies were purchased from Proteintech North America (Rosemont, IL 60018, USA). Other chemicals were of analytical or chromatographic grade.

Cell lines and animals

MRSA (ATCC29213) was purchased from Beijing Zhongke Quality Inspection Biotechnology Co., Ltd. BALB/c female mice (~ 18–22 g) were obtained from the Liaoning Changsheng Biological Co., Ltd. (Shenyang, China). This study was approved by the Ethics Committee of Liaoning University of Traditional Chinese Medicine in accordance with the institution's animal care and use guidelines (210000420230202). The experimental animals were cultured in the experimental center with free drinking water and food and natural light at 20–25 °C.

Investigation of synergistic effect

The Bliss independence model was used to determine drug synergy, and the synergy index was calculated using the following formula: $S = (F_x/F_0)\,(F_y/F_0) - (F_{xy}/F_0)$, where F_{xy} represents the bacterial growth rate with combined drug treatment, F_x and F_y represent the bacterial growth rates in the presence of x and y drugs, respectively, F_0 represents the bacterial growth rate without drug treatment, and S represents the synergy index[64]. The growth rate at different time points was determined by calculating the slope of the growth or inhibition curve.

Preparation of micelles

MagII-AZI/Cur-Ms were prepared using the thin-film hydration method[65–68]. $mPEG_{114}$-$PDPA_{10}$, $TPGS_{1000}$, DSPE-PEG_{2000}, DSPE-PEG_{2000}-MagII, AZI, and Cur were dissolved in methanol in a molar ratio of

114:132:7:4:13:54 and placed in a round-bottom flask. A rotary evaporator was used to dry the mixed solution at 40 °C for 10 min, forming a thin film. The film was hydrated with 5 mL of PBS for 20 min. After centrifuging the hydrate at 1.61×10^{-2} g for 10 min, the supernatant obtained by passing 0.22 μm polycarbonate membrane three times was micelle. Other formulations, including Blank-Ms, AZI-Ms, AZI/Cur-Ms, Cou-Ms, MagII-Cou-Ms, DiR-Ms, and MagII-DiR-Ms, were prepared using the same procedure.

Characterization of micelles

A transmission electron microscope (TEM, Tecnai G220ST; FEI Co., Tokyo, Japan) was used to observe the micellar morphology. The Z-average diameter size, PDI, and zeta potential of the micelles were measured using a Nano Series Zen 4003 Zetasizer (Litesizer 500; Anton Paar Instruments Ltd., Graz, Austria).

Pyrene was used as a fluorescence probe to determine the CMC. Pyrene solution and then various concentrations of Blank-Ms were added after natural drying in the dark overnight, ensuring the final pyrene concentration as 2×10^{-6} M. The test tubes were kept in the dark overnight, and the values were recorded at excitation wavelengths of 373 and 384 nm and an emission wavelength of 340 nm.

The EE was determined using high-performance liquid chromatography with an ultraviolet detector. The EE was calculated as follows: EE (%) = $(W_1/W) \times 100\%$, where W_1 is the amount of drug after passing through the 0.22-μm polycarbonate membrane, and W is the total amount of drug before centrifugation. MagII-AZI/Cur-Ms was stored at 4 °C and 25 °C for 20 days to evaluate micellar stability, with EE measured after 0, 5, 10, 15, and 20 days.

Colocalization of fluorescently labeled micelles and planktonic Bacteria

Cell uptake in different formulations was observed using confocal microscopy[69]. The bacterial suspension (1×10^8 CFU/mL) was incubated with Blank-Ms, Cou-Ms, and MagII-Cou-Ms for 4 h, where the final concentration of Cou was 3 μM. MRSA was washed three times with PBS and then fixed with 4% paraformaldehyde at room temperature for 10 min. The nuclei were stained in the dark with Hoechst 33,258 dye for 10 min. The bacteria were placed in confocal dishes and observed by spinning disk confocal microscope (HOOKE S3000, HOOKE Instruments Ltd, China). Finally, we use ImageJ software to measure fluorescence intensity in confocal microscopy imaging. The fluorescence intensity was quantified using ImageJ.

Determination of minimum inhibitory concentration

The MIC of MRSA for Blank-Ms, AZI-Ms, AZI/Cur-Ms, and MagII-AZI/Cur-Ms was determined using the microbroth dilution method. MRSA was inoculated into an Luria-Bertani (LB) solid medium and cultured at 37 °C for 24 h. A single colony was cultured in a liquid medium at 37 °C for 12 h. The MRSA was adjusted to 1×10^6 Colony-Forming Units/mL (CFU/mL) with the culture solution and added to the 96-well plate. The dosages of AZI in the formulation were 25, 18.75, 12.5, 10, 7.5, 5, 2.5, 1.25, and 0.625 μM, respectively. The mixed 96-well plate was incubated at 37 °C for 24 h, and the MIC of MRSA was the minimum concentration of the drug without bacterial growth.

Evaluation of antibacterial activity in vitro

Bacterial time-growth curves were used to observe MRSA growth. A bacterial suspension (1×10^6 CFU/mL) was incubated in 96-well plates at 37 °C for 24 h (the final concentration of AZI was 0.625 μM). The OD_{600} values were measured every 1 h with a multifunctional enzyme marker for 24 h, and the time-growth curve was plotted.

The bacteriostatic effects of different micelles were assessed by a bacteriostatic zone experiment. Bacterial suspensions (1×10^6 CFU/mL) were spread on plates, and a blank drug-sensitive paper was placed on the surface. Blank-Ms, AZI-Ms, AZI/Cur-Ms, and MagII-AZI/Cur-Ms were applied to the paper. The diameter of the antibacterial zone was measured vertically after 24 h.

The bacterial morphology after treatment with different preparations was observed using a SEM. The bacteria were fixed overnight with 2.5% glutaraldehyde solution at 4 °C and then dehydrated with 30%, 50%, 70%, 80%, and 90% ethanol for 15 min and with 100% ethanol for 20 min. The bacteria were dried in a Leica EM CPD300 critical point dryer (Leica Microsystems Wetzlar GmbH, German) and imaged with an Hitachi SU3500 scanning electron microscope (Hitachi, Ltd., Japan).

Destructive effect on biofilms

The activity of micelles in preventing the formation of bacterial biofilms was assessed using crystal violet staining. MRSA suspensions (1×10^6 CFU/mL) in the logarithmic growth phase were incubated in 96-well plates at 37 °C for 24 h ((the final concentration of AZI was 1.25 μM). The floating bacteria were removed, and the biofilms were stained with crystal violet. The biofilm was dissolved with 33% acetic acid, and optical density (OD) values at 595 nm were determined using a multifunctional enzyme analyzer (BioTek Synergy H1, Agilent Technologies Inc., America).

To visualize the cleaning effect on biofilms, treated biofilms were stained with SYTO 9 green fluorescent nucleic acid stain (SYTO-9) for live bacteria and Propidium Iodide (PI) for dead bacteria. MRSA suspensions (1×10^6 CFU/mL) were incubated on confocal dishes at 37 °C for 24 h. The biofilms were treated with Blank-Ms, AZI-Ms, AZI/Cur-Ms, and MagII-AZI/Cur-Ms at 37 °C for 3 h ((the final concentration of AZI was 1.25 μM)), washed three times with PBS buffer [containing SYTO-9 (2 μM) and PI (1 μM)], stained in the dark at room temperature for 15 min, and observed under the spinning disk confocal microscope.

Reactive oxygen species assays

ROS assays were conducted to explore the antimicrobial mechanisms of micelles. A bacterial suspension (1×10^6 CFU/mL) was resuspended in PBS and incubated with various formulations at 2 MIC in the dark for 4 h. MRSA

was stained with 2,7-dichlorodihydrofluorescein (DCFH-DA, 10 μM) at 37 °C in the dark for 30 min and washed three times with PBS. The OD value was determined at excitation and emission wavelengths of 485 and 535 nm, respectively using a multifunctional enzyme marker.

Evaluation of in vivo targeting

The targeting ability of micelles was investigated using small-animal in vivo imaging. Bacterial infection models of varying depths were established in BALB/c mice. The MRSA concentration in the logarithmic growth phase was adjusted to 1×10^8 CFU/mL. A skin infection model was constructed by injecting 100 μL of MRSA subcutaneously into the back of mice. A muscle infection model was constructed by the intramuscular injection of 100 μL of MRSA. The bacterial concentration was adjusted to 1×10^9 CFU/mL, and the bacterial pneumonia model was established by the nasal drop method. The mice were randomly divided into four groups 12 h. and treated with either normal saline, free DiR, DiR-Ms, or MagII- DiR-Ms via tail vein injection. In vivo fluorescence imaging system (IVScope 8200; Clinx, China) was used to observe the fluorescence distribution in mice with skin and muscle infections at 2, 6, 8, 10, 24, 48, 72, and 96 h post-anesthesia. The lungs of mice with pneumonia were resected 48 h after injection, and the fluorescence distribution in the lungs was observed.

Evaluation of pharmacodynamics in vivo

Mice in the same infection model were randomly assigned to four groups. Each group received one of the following treatments via tail vein injection: free AZI/Cur, AZI/Cur-Ms, MagII-AZI/Cur-Ms, or normal saline. The AZI concentration was maintained at 2.5 mg/mL and the free drug was dissolved in PBS containing 5% Dimethyl sulfoxide. The drug was administered once every other day for a total of three times. The weight of the mice was recorded after each administration. The expression levels of inflammatory cytokines were evaluated in the blood of mice with skin and muscle infections. The homogenates of infected parts of the skin or muscle tissue were cultured on an LB solid medium to evaluate the bacteriostatic effect. The skin or muscle tissue was embedded in paraffin wax and cut into 3- to 5-μm-thick sections. Hematoxylin–eosin (HE) staining was used to examine cell density, and Masson staining was performed to investigate tissue distribution. Similarly, the cells of the BALF of mice with pneumonia were counted using Reye's staining, and the expression of inflammatory cytokines in BALF was investigated. After the mice were sacrificed, their lungs were embedded in paraffin wax and cut into 3- to 5-μm-thick slices. The expression of inflammation-related proteins, including C5aR1, C5b-9, C3c, and NF-κB p65, was examined by immunofluorescence. In simple terms, deparaffinize the sections to water and perform antigen retrieval. Block non-specific binding sites with 5% bovine serum albumin (BSA), and then incubate with the primary antibody (C5aR1, C5b-9, C3c, and NF-κB p65) overnight at 4 °C. After that, carry out the secondary antibody incubation while avoiding light. Thoroughly wash the sections with PBS buffer after each step. Finally, stain the nuclei with DAPI. Observe and capture images of the mounted sections under a fluorescence microscope. Use Image J software to quantitatively analyze the fluorescence intensity.

Statistical analysis

The data were analyzed using GraphPad Prism software and presented as mean ± standard deviation. One-way analysis of variance was used to evaluate significant differences among sample groups. A P value < 0.05 indicated a statistically significant difference.

Conclusions

In this study, MagII-modified AZI and Cur micelles were prepared, and their targeting and antibacterial effects in models of bacterial infection at various depths were evaluated. MagII-AZI/Cur-Ms demonstrated excellent targeting and antibacterial efficacy due to several factors. First, the insoluble drugs were encapsulated in micelles, and the micellar surface was modified with long-circulating materials, extending their action in vivo. Second, the combination of AZI and Cur increased the antibacterial activity while reducing bacterial resistance. Finally, the modification of antimicrobial peptide MagII enabled micelles to actively target bacterial infection sites at different depths of the body, increasing drug accumulation at bacterial infection sites. These findings provide valuable insights for combating drug-resistant bacteria; however, their potential clinical applications warrant further investigation.

Data availability

Data is provided within the manuscript and supplementary information files. The data that support the findings of this study are available from the corresponding author upon reasonable request.

Received: 27 November 2024; Accepted: 27 February 2025
Published online: 03 March 2025

References

1. Xu, W., Qing, X., Liu, S., Chen, Z. & Zhang, Y. Manganese oxide nanomaterials for bacterial infection detection and therapy. *J. Mater. Chem. B* **10**, 1343–1358. https://doi.org/10.1039/d1tb02646a (2022).
2. Ahmad-Mansour, N. et al. Staphylococcus aureus toxins: An update on their pathogenic properties and potential treatments. *Toxins* **13**. https://doi.org/10.3390/toxins13100677 (2021).
3. Gil, E., Noursadeghi, M. & Brown, J. S. Streptococcus pneumoniae interactions with the complement system. *Front. Cell. Infect. Microbiol.* **12**, 929483. https://doi.org/10.3389/fcimb.2022.929483 (2022).
4. Tarin-Pello, A., Suay-Garcia, B. & Perez-Gracia, M. T. Antibiotic resistant bacteria: Current situation and treatment options to accelerate the development of a new antimicrobial arsenal. *Expert Rev. Anti Infect. Ther.* **20**, 1095–1108. https://doi.org/10.1080/14787210.2022.2078308 (2022).

5. Uddin, T. M. et al. Antibiotic resistance in microbes: History, mechanisms, therapeutic strategies and future prospects. *J. Infect. Public. Health* **14**, 1750–1766. https://doi.org/10.1016/j.jiph.2021.10.020 (2021).
6. Uruen, C., Garcia, C., Fraile, L., Tommassen, J. & Arenas, J. How Streptococcus suis escapes antibiotic treatments. *Vet. Res.* **53**, 91. https://doi.org/10.1186/s13567-022-01111-3 (2022).
7. Makabenta, J. M. V. et al. Nanomaterial-based therapeutics for antibiotic-resistant bacterial infections. *Nat. Rev. Microbiol.* **19**, 23–36. https://doi.org/10.1038/s41579-020-0420-1 (2021).
8. Hatlen, T. J. & Miller, L. G. Staphylococcal skin and soft tissue infections. *Infect. Dis. Clin. North. Am.* **35**, 81–105. https://doi.org/10.1016/j.idc.2020.10.003 (2021).
9. Yao, H. et al. Pathogen-Targeting bimetallic nanozymes as Ultrasonic-Augmented ROS generator against multidrug resistant bacterial infection. *Adv. Healthc. Mater.* **12**, e2300449. https://doi.org/10.1002/adhm.202300449 (2023).
10. Kern, W. V. & Rieg, S. Burden of bacterial bloodstream infection-a brief update on epidemiology and significance of multidrug-resistant pathogens. *Clin. Microbiol. Infect.* **26**, 151–157. https://doi.org/10.1016/j.cmi.2019.10.031 (2020).
11. Coates, A. R. M., Hu, Y., Holt, J. & Yeh, P. Antibiotic combination therapy against resistant bacterial infections: Synergy, rejuvenation and resistance reduction. *Expert Rev. Anti Infect. Ther.* **18**, 5–15. https://doi.org/10.1080/14787210.2020.1705155 (2020).
12. Firth, A., Prathapan, P. & Azithromycin: The first broad-spectrum therapeutic. *Eur. J. Med. Chem.* **207**, 112739. https://doi.org/10.1016/j.ejmech.2020.112739 (2020).
13. Oliver, M. E. & Hinks, T. S. C. Azithromycin in viral infections. *Rev. Med. Virol.* **31**, e2163. https://doi.org/10.1002/rmv.2163 (2021).
14. Peng, Y. et al. Anti-inflammatory effects of Curcumin in the inflammatory diseases: Status, limitations and countermeasures. *Drug Des. Devel Ther.* **15**, 4503–4525. https://doi.org/10.2147/DDDT.S327378 (2021).
15. Sanchez-Salcedo, S., Heras, C., Lozano, D., Vallet-Regi, M. & Salinas, A. J. Nanodevices based on mesoporous glass nanoparticles enhanced with zinc and Curcumin to fight infection and regenerate bone. *Acta Biomater.* **166**, 655–669. https://doi.org/10.1016/j.actbio.2023.04.046 (2023).
16. Zia, A., Farkhondeh, T., Pourbagher-Shahri, A. M. & Samarghandian, S. The role of curcumin in aging and senescence: Molecular mechanisms. *Biomed. Pharmacother.* **134**, 111119. https://doi.org/10.1016/j.biopha.2020.111119 (2021).
17. Xu, T. et al. Application of curcumin and its derivatives in tumor multidrug resistance. *Phytother. Res.* **34**, 2438–2458. https://doi.org/10.1002/ptr.6694 (2020).
18. Hwang, D., Ramsey, J. D. & Kabanov, A. V. Polymeric micelles for the delivery of poorly soluble drugs: From nanoformulation to clinical approval. *Adv. Drug Deliv Rev.* **156**, 80–118. https://doi.org/10.1016/j.addr.2020.09.009 (2020).
19. Ghezzi, M. et al. Polymeric micelles in drug delivery: An insight of the techniques for their characterization and assessment in biorelevant conditions. *J. Control Release* **332**, 312–336. https://doi.org/10.1016/j.jconrel.2021.02.031 (2021).
20. Baptista, B. et al. pH-responsive nanoparticles based on POEOMA-b-PDPA block copolymers for RNA encapsulation, protection and cell delivery. *Biomater. Adv.* **145**, 213267. https://doi.org/10.1016/j.bioadv.2022.213267 (2023).
21. Ding, N. et al. A cyclodextrin-based pH-responsive MicroRNA delivery platform targeting polarization of M1 to M2 macrophages for sepsis therapy. *Adv. Healthc. Mater.* **12**, e2301243. https://doi.org/10.1002/adhm.202301243 (2023).
22. Ding, F. et al. Antifouling and pH-responsive poly(carboxybetaine)-based nanoparticles for tumor cell targeting. *Front. Chem.* **7**, 770. https://doi.org/10.3389/fchem.2019.00770 (2019).
23. Dong, Y. & Liu, P. Improving drug delivery performance of pH-triggered prodrug nanoparticles with an adaptive polycation block as pH-sensitive gatekeeper. *Int. J. Pharm.* **589**, 119796. https://doi.org/10.1016/j.ijpharm.2020.119796 (2020).
24. Jia, C. et al. Preparation of dual-template epitope imprinted polymers for targeted fluorescence imaging and targeted drug delivery to pancreatic cancer BxPC-3 cells. *ACS Appl. Mater. Interfaces* **11**, 32431–32440. https://doi.org/10.1021/acsami.9b11533 (2019).
25. Luo, Y., Yang, H., Zhou, Y. F. & Hu, B. Dual and multi-targeted nanoparticles for site-specific brain drug delivery. *J. Control Release* **317**, 195–215. https://doi.org/10.1016/j.jconrel.2019.11.037 (2020).
26. Fan, X. L. et al. Magainin-modified polydopamine nanoparticles for photothermal killing of bacteria at low temperature. *Colloids Surf. B Biointerfaces* **183**, 110423. https://doi.org/10.1016/j.colsurfb.2019.110423 (2019).
27. McMillan, K. A. M., Coombs, M. R. P. & Review: Examining the natural role of amphibian antimicrobial peptide Magainin. *Molecules* **25**. https://doi.org/10.3390/molecules25225436 (2020).
28. Demidenko, E. & Miller, T. W. Statistical determination of synergy based on bliss definition of drugs independence. *PLoS ONE* **14**, e0224137. https://doi.org/10.1371/journal.pone.0224137 (2019).
29. Howell, M. et al. Exploring synergy and its role in antimicrobial peptide biology. *Methods Enzymol.* **663**, 99–130. https://doi.org/10.1016/bs.mie.2021.09.017 (2022).
30. Baeder, D. Y., Yu, G., Hoze, N., Rolff, J. & Regoes, R. R. Antimicrobial combinations: Bliss independence and Loewe additivity derived from mechanistic multi-hit models. *Philos. Trans. R. Soc. Lond. B Biol. Sci.* **371**. https://doi.org/10.1098/rstb.2015.0294 (2016).
31. Li, H., Hu, D., Liang, F., Huang, X. & Zhu, Q. Influence factors on the critical micelle concentration determination using pyrene as a probe and a simple method of preparing samples. *R. Soc. Open Sci.* **7**, 192092. https://doi.org/10.1098/rsos.192092 (2020).
32. Lei, L. et al. The self-assembled Zein hydrolysate-curcumin nanocomplex: Improvement on the stability and sustainable release of curcumin. *J. Sci. Food Agric.* **102**, 5729–5737. https://doi.org/10.1002/jsfa.11922 (2022).
33. Feng, X. et al. Anti-HER2 immunoliposomes: Antitumor efficacy attributable to targeted delivery of anthraquinone-fused enediyne. *Adv. Sci.* e2307865. https://doi.org/10.1002/advs.202307865 (2024)
34. Gesell, J., Zasloff, M. & Opella, S. J. Two-dimensional 1H NMR experiments show that the 23-residue magainin antibiotic peptide is an alpha-helix in Dodecylphosphocholine micelles, sodium dodecylsulfate micelles, and trifluoroethanol/water solution. *J. Biomol. NMR* **9**, 127–135. https://doi.org/10.1023/a:1018698002314 (1997).
35. Semeraro, E. F. et al. Magainin 2 and PGLa in bacterial membrane mimics IV: Membrane curvature and partitioning. *Biophys. J.* **121**, 4689–4701. https://doi.org/10.1016/j.bpj.2022.10.018 (2022).
36. Rukavina, Z., Segvic Klaric, M., Filipovic-Grcic, J., Lovric, J. & Vanic, Z. Azithromycin-loaded liposomes for enhanced topical treatment of methicillin-resistant Staphyloccocus aureus (MRSA) infections. *Int. J. Pharm.* **553**, 109–119. https://doi.org/10.1016/j.ijpharm.2018.10.024 (2018).
37. Batista, A. et al. Anti-MRSA activity of Curcumin in planktonic cells and biofilms and determination of possible action mechanisms. *Microb. Pathog.* **155**, 104892. https://doi.org/10.1016/j.micpath.2021.104892 (2021).
38. Yadav, M. K., Singh, B. & Tiwari, S. K. Comparative analysis of inhibition-based and indicator-independent colorimetric assay for screening of bacteriocin-producing lactic acid bacteria. *Probiotics Antimicrob. Proteins* **11**, 687–695. https://doi.org/10.1007/s12602-018-9445-4 (2019).
39. Hoiby, N. et al. Formation of Pseudomonas aeruginosa inhibition zone during tobramycin disk diffusion is due to transition from planktonic to biofilm mode of growth. *Int. J. Antimicrob. Agents* **53**, 564–573. https://doi.org/10.1016/j.ijantimicag.2018.12.015 (2019).
40. Cheah, Y. T. & Chan, D. J. C. Physiology of microalgal biofilm: A review on prediction of adhesion on substrates. *Bioengineered* **12**, 7577–7599. https://doi.org/10.1080/21655979.2021.1980671 (2021).
41. Fulaz, S., Vitale, S., Quinn, L. & Casey, E. Nanoparticle-biofilm interactions: The role of the EPS matrix. *Trends Microbiol.* **27**, 915–926. https://doi.org/10.1016/j.tim.2019.07.004 (2019).
42. Vuotto, C. & Donelli, G. Novel treatment strategies for biofilm-based infections. *Drugs* **79**, 1635–1655. https://doi.org/10.1007/s40265-019-01184-z (2019).

43. Yin, W., Wang, Y., Liu, L., He, J. & Biofilms: The microbial protective clothing in extreme environments. *Int. J. Mol. Sci.* **20**. https://doi.org/10.3390/ijms20143423 (2019).
44. Solano, C., Echeverz, M. & Lasa, I. Biofilm dispersion and quorum sensing. *Curr. Opin. Microbiol.* **18**, 96–104. https://doi.org/10.1016/j.mib.2014.02.008 (2014).
45. Sharma, D., Misba, L. & Khan, A. U. Antibiotics versus biofilm: An emerging battleground in microbial communities. *Antimicrob. Resist. Infect. Control* **8**, 76. https://doi.org/10.1186/s13756-019-0533-3 (2019).
46. Grande, R., Puca, V. & Muraro, R. Antibiotic resistance and bacterial biofilm. *Expert Opin. Ther. Pat.* **30**, 897–900. https://doi.org/10.1080/13543776.2020.1830060 (2020).
47. Yan, J. & Bassler, B. L. Surviving as a community: Antibiotic tolerance and persistence in bacterial biofilms. *Cell. Host Microbe* **26**, 15–21. https://doi.org/10.1016/j.chom.2019.06.002 (2019).
48. Qiao, Z. et al. Antibiofilm effects of bacteriocin BMP32r on listeria monocytogenes. *Probiotics Antimicrob. Proteins* **14**, 1067–1076. https://doi.org/10.1007/s12602-021-09863-8 (2022).
49. Gonzalez, A. et al. Characterization and antimicrobial effect of a bioinspired thymol coating formed on titanium surface by one-step immersion treatment. *Dent. Mater.* **36**, 1495–1507. https://doi.org/10.1016/j.dental.2020.09.006 (2020).
50. Diaz-Garcia, D. et al. Copper-functionalized nanostructured silica-based systems: Study of the antimicrobial applications and ROS generation against gram positive and gram negative bacteria. *J. Inorg. Biochem.* **203**, 110912. https://doi.org/10.1016/j.jinorgbio.2019.110912 (2020).
51. Li, J. et al. Acidic biofilm microenvironment-responsive ROS generation via a protein nanoassembly with hypoxia-relieving and GSH-depleting capabilities for efficient elimination of biofilm bacteria. *Acta Biomater.* **186**, 439–453. https://doi.org/10.1016/j.actbio.2024.07.044 (2024).
52. Alomary, M. N. & Ansari, M. A. Proanthocyanin-capped biogenic TiO(2) nanoparticles with enhanced penetration, antibacterial and ROS mediated inhibition of bacteria proliferation and biofilm formation: A comparative approach. *Chemistry* **27**, 5817–5829. https://doi.org/10.1002/chem.202004828 (2021).
53. Azzopardi, E. A., Ferguson, E. L. & Thomas, D. W. The enhanced permeability retention effect: A new paradigm for drug targeting in infection. *J. Antimicrob. Chemother.* **68**, 257–274. https://doi.org/10.1093/jac/dks379 (2013).
54. Chen, Z. et al. Enhancing the treatment of uncontrolled inflammation through the targeted delivery of TPCA-1-loaded nanoparticles. *Pharmaceutics* **15**. https://doi.org/10.3390/pharmaceutics15102435 (2023).
55. Virzi, N. F. et al. Curcumin I-SMA nanomicelles as promising therapeutic tool to tackle bacterial infections. *RSC Adv.* **13**, 31059–31066. https://doi.org/10.1039/d3ra04885c (2023).
56. Tang, Q. et al. Remodel heterogeneous electrical microenvironment at nano-scale interface optimizes osteogenesis by coupling of immunomodulation and angiogenesis. *Small* e2406090. https://doi.org/10.1002/smll.202406090 (2024).
57. Kanaujiya, S. et al. Resveratrol-ampicillin dual-drug loaded polyvinylpyrrolidone/polyvinyl alcohol biomimic electrospun nanofiber enriched with collagen for efficient burn wound repair. *Int. J. Nanomed.* **19**, 5397–5418. https://doi.org/10.2147/IJN.S464046 (2024).
58. Jiao, Y. et al. Flavonoid substituted polysaccharides from Tamarix chinensis Lour. Alleviate H1N1-induced acute lung injury via inhibiting complement system. *J. Ethnopharmacol.* **322**, 117651. https://doi.org/10.1016/j.jep.2023.117651 (2024).
59. Friscic, J. et al. The complement system drives local inflammatory tissue priming by metabolic reprogramming of synovial fibroblasts. *Immunity* **54**, 1002–1021. https://doi.org/10.1016/j.immuni.2021.03.003 (2021).
60. Desai, J. V. et al. C5a-licensed phagocytes drive sterilizing immunity during systemic fungal infection. *Cell* **186**, 2802–2822 e2822. https://doi.org/10.1016/j.cell.2023.04.031 (2023).
61. Lin, S. et al. Rhamnolipid micelles assist azithromycin in efficiently disrupting Staphylococcus aureus biofilms and impeding their re-formation. *Int. J. Nanomed.* **18**, 7403–7415. https://doi.org/10.2147/IJN.S436971 (2023).
62. Bendary, M. M. et al. Boosting the anti-helicobacter efficacy of azithromycin through natural compounds: Insights from in vitro, in vivo, histopathological, and molecular docking investigations. *Helicobacter* **29**, e13110. https://doi.org/10.1111/hel.13110 (2024).
63. Yuanyuan Wang, B. X., Jiang, L., Liu, J. Y. Z., Li, S. & Liu, D. Antimicrobial peptide-modified pH-sensitive micelles against pneumonia caused by methicillin-resistant Staphylococcus aureus. *J. Drug Deliv. Sci. Technol.* **98**, 105875. https://doi.org/10.1016/j.jddst.2024.105875 (2024).
64. Hegreness, M., Shoresh, N., Damian, D., Hartl, D. & Kishony, R. Accelerated evolution of resistance in multidrug environments. *Proc. Natl. Acad. Sci. U S A* **105**, 13977–13981. https://doi.org/10.1073/pnas.0805965105 (2008).
65. Guo, R. B. et al. Folate-modified triptolide liposomes target activated macrophages for safe rheumatoid arthritis therapy. *Biomater. Sci.* **10**, 499–513. https://doi.org/10.1039/d1bm01520f (2022).
66. Wang, J. et al. Multifunctional Icariin and Tanshinone IIA co-delivery liposomes with potential application for Alzheimer's disease. *Drug Deliv.* **29**, 1648–1662. https://doi.org/10.1080/10717544.2022.2072543 (2022).
67. Li, F. R. et al. Borneol-modified schisandrin B micelles cross the blood-brain barrier to treat Alzheimer's disease in aged mice. *ACS Chem. Neurosci.* **15**, 593–607. https://doi.org/10.1021/acschemneuro.3c00625 (2024).
68. Liu, Y. et al. Borneol-modified docetaxel plus tetrandrine micelles for treatment of drug-resistant brain glioma. *Drug Dev. Ind. Pharm.* **50**, 135–149. https://doi.org/10.1080/03639045.2024.2302886 (2024).
69. Meng, Y. et al. Multi-functional liposomes enhancing target and antibacterial immunity for antimicrobial and anti-biofilm against methicillin-resistant Staphylococcus aureus. *Pharm. Res.* **33**, 763–775. https://doi.org/10.1007/s11095-015-1825-9 (2016).

Acknowledgements

The authors thank Liaoning University of Traditional Chinese Medicine for providing suggestions on the use of SU3500 scanning electron microscopy, confocal microscopy and small animal live imager. This work was supported by the Open fund of Key Laboratory of Ministry of Education for TCM Viscera-State Theory and Applications, Liaoning University of Traditional Chinese Medicine [Grant No.zyzx2301], China Postdoctoral Science Foundation [Grant No. 2022MD723796], the Doctoral Start-up Foundation of Liaoning Province [Grant No. 2023-BS-139], Basic Research Project of Education Department of Liaoning Province [Grant No. JYTQN 2023471], the National Natural Science Foundation of China [Grant No.82204629] and the Liaoning Province Natural Science Foundation doctoral foundation [Grant No. 2022-BS-197].

Author contributions

L.Z.: Writing—original draft, Validation, Writing—review and editing. R.G.: Data curation, Software. Y.L.: Methodology. L.K.: Supervision, Funding acquisition. J.Z.: Supervision. Z.Z.: Visualization. J.W.: Project administration. M.C.: Data curation. M.L.: Methodology. Y.Y.: Writing—review and editing, Funding acquisition. X.L.: Writing—review and editing, Methodology.

Declarations

Ethics approval and consent to participate

This study is approved by the Ethics Committee of Liaoning University of Traditional Chinese Medicine in accordance with the institution's animal care and use guidelines (210000420230202). The study is reported in accordance with the ARRIVE guidelines.

Competing interests

The authors declare no competing interests.

Additional information

Supplementary Information The online version contains supplementary material available at https://doi.org/10.1038/s41598-025-92384-z.

Correspondence and requests for materials should be addressed to Y.Y. or X.-t.L.

Reprints and permissions information is available at www.nature.com/reprints.

Publisher's note Springer Nature remains neutral with regard to jurisdictional claims in published maps and institutional affiliations.